Fast Imaging Method for Security Systems using Ultrawideband Radar

TAKUYA SAKAMOTO, Member, IEEE
University of Hyogo
Himeji, Japan

TORU SATO, Member, IEEE
Kyoto University
Kyoto, Japan

PASCAL AUBRY
ALEXANDER YAROVOY, Fellow, IEEE
Delft University of Technology
Delft, The Netherlands

We propose a fast method of ultrawideband (UWB) radar imaging that can be applied to a moving target, having in mind such application as concealed weapon detection. We demonstrate the performance of the proposed method using simulations and measurements with static and moving targets. We also compare the computational complexity of the proposed method with that of a conventional method to clarify the feasibility of applying the proposed method to the intended real-time systems.

Manuscript received March 3, 2014; revised April 10, 2015; released for publication October 4, 2015.

DOI. No. 10.1109/TAES.2015.140167.

Refereeing of this contribution was handled by C. Baker.

This study was supported in part by the Supporting Program for Interaction-based Initiative Team Studies (SPIRITS), Japan-Netherlands joint development of sleep monitoring technology using UWB radar, the Japan Society for the Promotion of Science Postdoctoral Fellowships for Research Abroad (high-resolution imaging for human bodies with UWB radar using multipath echoes), the Center of Innovation Program (the last 5X innovation R&D center for a smart, happy, and resilient society), JSPS KAKENHI Grants (25249057 and 15K18077), and the R&D project for expansion of radio spectrum resources for more efficient use of frequency resources for the future (The Ministry of Internal Affairs and Communications, Japan).

Authors' addresses: T. Sakamoto, University of Hyogo, Graduate School of Engineering, 2167 Shosha, Himeji, 671-2280, Japan; T. Sato, Kyoto University, Graduate School of Informatics, Yoshida-Honmachi, Sakyo-ku, Kyoto, 606-8501, Japan; P. Aubry, A. Yarvoy, Delft University of Technology, Microelectronics, TU Delft EEMCS Building, Mekelweg 4, Delft, CD 2628, The Netherlands. Corresponding author is T. Sakamoto, E-mail: (t-sakamo@i.kyoto-u.ac.jp).

I. INTRODUCTION

Protection of civilians from terrorist threats has become a high priority in society. Because terrorists are developing increasingly sophisticated schemes to circumvent public space screening, there is a need to implement enhanced security measures at public areas and in particular at airports. Radar imaging is a key element in these efforts because the method provides crucial abilities such as accurate ranging, concealed object classification via imaging and penetration through clothing and walls.

Radar imaging has been applied for security purposes to the indoor tracking of people [1, 2], nondestructive testing [3, 4] and through-the-wall imaging [5]. Above all, however, radar-based weapon detection is one of the most active topics in the radar-imaging field. Unlike X-rays, radar waves do not pose health risks because they do not ionize human tissue, while providing reasonable spatial resolution and penetrability.

While the use of terahertz radar is a promising candidate technology for this purpose [6–8], its high cost prevents the widespread use of this technology. In contrast, microwave and millimeter-wave radar can be realized using relatively low-cost devices, and they have both penetration capability and sufficient spatial resolution for weapon detection [9, 10]. Detection of weapons without imaging has also been studied [11, 12], but imaging-based weapon detection has been studied more intensively [10, 13, 14] and as a result has been commercialized, and is widely used in the form of microwave-based body scanners (e.g., ProVision2 from L-3 Communications, NY).

These body scanners require the person under investigation to remain stationary during the measurement process. This measurement takes a nonnegligible time because many such devices mechanically scan their antennas. Therefore, if the person to be measured is in motion, the resulting images become blurred. If this problem is overcome, then one can develop an unobtrusive prescreening system for moving people [15].

Many studies have been performed on imaging of moving targets in the far-field [16, 17]. Images of targets in the far-field are formed by compensating for the phase shift. In contrast, the scattering center of a near-field target depends on both the target shape and the antenna position, which cannot be easily estimated. Therefore, it is difficult to apply the conventional imaging methods that were designed for far-field targets to a near-field target.

In this paper, we propose an autofocusing near-field imaging method that avoids blurriness. To this end, we first generate multiple images by assuming various target speeds, and then find the most focused image. The largest hurdle when applying this method is the computational time, because the imaging process must be repeated multiple times. This hinders the system throughput, which is one of the most important characteristics required for passenger screening systems.

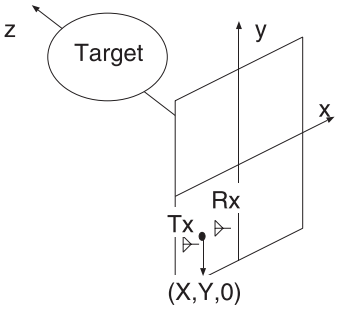

Fig. 1. System model with pair of antennas scanning from ($z = 0$) plane.

In many radar imaging applications, including body scanners, the F-K (frequency-wavenumber) migration [18] has been commonly used, because it offers reasonable resolution and fast computation when using a fast Fourier transform (FFT) algorithm. For a moving target, however, the imaging process must be performed numerous times, which drives the need for an even faster imaging method. Because the computational speed of the F-K migration is restricted by the speed of the FFT, it is therefore necessary to introduce a completely different approach that does not use an FFT.

To overcome the limitation mentioned above, we propose a fast imaging method, revised range point migration (RRPM), that uses a combination of a reversible transform, the inverse boundary scattering transform (IBST) [19–21], and another robust imaging method called range point migration (RPM) [22]. It has been reported in the literature that RPM is faster than the time-domain delay-and-sum migration, and that RRPM is even faster than RPM. Preliminary parts of this study have been published [23–27]. This paper presents a performance comparison between the F-K migration, RPM, and RRPM in terms of image quality and computational speed to assess the feasibility of imaging of a moving near-field target with sufficient resolution for weapon detection. The imaging methods are applied to both simulation data and measurement data for a mannequin and a handgun to clarify their imaging capabilities and the associated computational complexity. Imaging of a moving weapon is also demonstrated using the RRPM to verify the image quality.

II. SYSTEM MODEL

Fig. 1 shows the three-dimensional ultrawideband (UWB) radar imaging system model assumed in this study. The measurement system consists of a transmitter–receiver pair positioned in the $z = 0$ plane along the x axis at a fixed distance $2d$. The midpoint between the transmitter and receiver is located at $(X, Y, 0)$, which means the transmitting and receiving antennas are located at $(X - d, Y, 0)$ and $(X + d, Y, 0)$, respectively. With the transmitter-receiver pair being rastered at discrete intervals across a portion of the $z = 0$ plane, UWB pulses are transmitted and pulse echoes are received. The received signals contain not only echoes from the target but also a coupling signal propagating directly from the transmitter to the receiver. To eliminate this coupling signal, the background signal, measured without the target prior to the actual measurement, is subtracted from the received signal. As we consider an application to a body scanner, the propagation environment is assumed to be free space, in which we do not assume other targets or clutters.

Given the antenna midpoint of $(X, Y, 0)$, the signal received is pulse-compressed and is stored as $s(X, Y, Z)$, where $Z = ct/2$. Here, c is the speed of the electromagnetic waves, and t is the time interval between transmission and reception. The pulse compression is realized by using a matched filter. We assume that the signal bandwidth is wide enough for the time-domain echoes to be well resolved in the radial direction. Because the pulse-compressed waveform is approximately the autocorrelation function of the transmitted waveform, as long as the bandwidth is sufficiently wide, most of the power of the pulse-compressed echo is localized within a narrow time span. For this reason, the transmitted waveform is arbitrary and can be composed of chirp, impulse, or code-modulated signals. However, no matter what signal waveform is used, the received radar data must go through a preprocessing stage for pulse compression to obtain the signal $s()$. Initially, we assume that the target is stationary. Later, we discuss the case with a moving target.

III. SEABED METHOD AND BISTATIC-IBST

This section explains the bistatic-IBST [21] that describes the mapping from the target range to a target surface image. This transform has been used in an imaging algorithm called SEABED [28], which is known to be fast in imaging single simple-shaped targets. In SEABED, we first extract peaks from received signals using the criteria

$$|s(X, Y, Z)| > T_s, \tag{1}$$

$$\frac{\partial}{\partial Z} s(X, Y, Z) = 0, \tag{2}$$

where T_s is a constant threshold introduced to suppress peaks caused by noise. These peaks are indexed as (X_i, Y_i, Z_i) for $(i = 1, 2, \ldots, N)$. The corresponding values of these peaks are for simplicity denoted $s_i = s(X_i, Y_i, Z_i)$. The value s_i takes a real value that can be positive or negative. For a single simple-shaped target, these points are easily connected sequentially to form multiple curved surfaces $Z(X, Y)$. Such a surface is called a quasi-wavefront.

Next, we apply the following bistatic-IBST to the quasi-wavefronts to obtain images,

$$x = X - \frac{2Z^3 Z_X}{Z^2 - d^2 + \sqrt{(Z^2 - d^2)^2 + 4d^2 Z^2 Z_X^2}}, \tag{3}$$

$$y = Y + Z_Y \left\{ d^2 (x - X)^2 - Z^4 \right\} / Z^3, \tag{4}$$

$$z=\sqrt{Z^2-d^2-(y-Y)^2-\frac{(Z^2-d^2)(x-X)^2}{Z^2}}, \quad (5)$$

using for simplicity $Z_X=\partial Z/\partial X$ and $Z_Y=\partial Z/\partial Y$.

The variables needed to apply the bistatic-IBST are X, Y, Z, Z_X, and Z_Y, of which X, Y, and Z are known. To obtain derivatives Z_X and Z_Y, peaks need to be connected when forming curved surfaces. Because this is not an easy task for complex-shaped targets, we defer using the bistatic-IBST alone.

IV. CONVENTIONAL RPM METHOD

The RPM has been developed to mitigate difficulties with SEABED [22]. This method was designed to optimize an evaluation function for estimating the direction of arrival of an echo. The RPM uses numerous signal peaks in this optimization process for calculating stable images. In this section, we describe the RPM using the bistatic-IBST. First, we define a weighting coefficient for a pair of peaks satisfying $s_i s_j>0$ as

$$w_{i,j}=\left|s_i s_j\right|\exp\left(-\frac{(X_i-X_j)^2}{2\sigma_X^2}-\frac{(Y_i-Y_j)^2}{2\sigma_Y^2}-\frac{(Z_i-Z_j)^2}{2\sigma_Z^2}\right), \quad (6)$$

where σ_X and σ_Y are scaling factors that determine the width of the Gaussian function. For a pair of peaks with $s_i s_j<0$, the weight is defined as $w_{i,j}=0$. Note again here that s_i has a real value and can either be positive or negative. This weight $w_{i,j}$ determines how much the j-th signal peak contributes in calculating the derivative at the i-th peak.

We calculate the derivative Z_X required for the bistatic-IBST in (3) as $Z_X=\tan(\hat{\theta}_i)$ for the i-th peak point, where $\hat{\theta}_i$ is the solution to the following optimization:

$$\hat{\theta}_i=\arg\max_{\theta_i} F(\theta_i), \quad (7)$$

$$F(\theta_i)=\sum_{j\neq i} w_{i,j}\exp\left(-\frac{\left(\theta_i-\tan^{-1}\left(\frac{Z_i-Z_j}{X_i-X_j}\right)\right)^2}{2\sigma_\theta^2}\right), \quad (8)$$

$$\text{subject to } |\theta_i|<\pi/4,$$

where σ_θ is a scaling factor that determines the width of each Gaussian function. The summation is calculated only for j satisfying $Y_j=Y_i$. By finding the optimum θ_i that maximizes (8), we obtain an estimate of the quasi-wavefront orientation. In a similar way, we can estimate Z_Y by replacing $(Z_i-Z_j)/(X_i-X_j)$ with $(Z_i-Z_j)/(Y_i-Y_j)$. Finally, these derivatives are substituted into (3), (4), and (5), to obtain target images (x, y, z).

V. PROPOSED RRPM METHOD

In this section, we propose a revised version of the RPM, called the RRPM. Although the RPM has been demonstrated to be efficient in imaging even complex target shapes [22], the method sacrifices processing speed. Because the optimization process of the function in (8) is time consuming, we replace this process by weighted averaging.

In the RPM, one must perform the following optimization to estimate the optimum $\theta=\theta_i$ as

$$\text{maximize } F(\theta)=\sum_j w_{i,j}\exp\left(-\frac{(\theta-\bar{\theta}_{i,j})^2}{2\sigma_\theta^2}\right), \quad (9)$$

where $\bar{\theta}_{i,j}=\tan^{-1}(\frac{Z_i-Z_j}{X_i-X_j})$ is defined for simplicity. If the function $F(\theta)$ has only a single peak, then the optimum value $\hat{\theta}$ can be obtained as $\mathrm{d}F(\theta)/\mathrm{d}\theta|_{\theta=\hat{\theta}}=0$, which means

$$\sum_j w_{i,j}(\hat{\theta}-\bar{\theta}_{i,j})\exp\left(-\frac{(\hat{\theta}-\bar{\theta}_{i,j})^2}{2\sigma_\theta^2}\right)=0. \quad (10)$$

By transforming (10), one obtains

$$\hat{\theta}=\frac{\sum_j w_{i,j}\theta_{i,j}\exp\left(-\frac{(\hat{\theta}-\bar{\theta}_{i,j})^2}{2\sigma_\theta^2}\right)}{\sum_j w_{i,j}\exp\left(-\frac{(\hat{\theta}-\bar{\theta}_{i,j})^2}{2\sigma_\theta^2}\right)}. \quad (11)$$

If the condition $\bar{\theta}_{i,j}\simeq\hat{\theta}$ is satisfied for all i and j, then one can approximate

$$\exp\left(-\frac{(\hat{\theta}-\bar{\theta}_{i,j})^2}{2\sigma_\theta^2}\right)\simeq 1. \quad (12)$$

This approximation leads to the expression

$$\hat{\theta}\simeq\frac{\sum_j w_{i,j}\theta_{i,j}}{\sum_j w_{i,j}}, \quad (13)$$

which is the basis of the proposed RRPM.

In the RRPM, the relative orientation of the peaks around the i-th peak is estimated as a weighted average

$$\hat{\theta}_i=\frac{\sum_{j\neq i, Y_j=Y_i}\tilde{w}_{i,j}\tan^{-1}\left(\frac{Z_i-Z_j}{X_i-X_j}\right)}{\sum_{j\neq i, Y_j=Y_i} w_{i,j}}, \quad (14)$$

where $\tilde{w}_{i,j}$ is a modified weight, and the summations are over pairs of peaks with the same sign $s_i s_j>0$ like in the RPM.

The modified weight is $\tilde{w}_{i,j}=\alpha_{i,j}w_{i,j}$, where we define

$$\alpha_{i,j}=\left(\frac{\min\{|s_i|,|s_j|\}}{\max\{|s_i|,|s_j|\}}\right)^p, \quad (15)$$

with a constant $p>1$. The term $\alpha_{i,j}$ suppresses the contribution of the j-th peak in calculating the derivative at the i-th peak if the amplitudes s_i and s_j are not close to each other. This term is needed because signal amplitudes should be similar at neighboring peak points unless there is a strong interference.

Fig. 2 is a schematic of the procedure of the RRPM. As in dictated, the inclination of points around the i-th

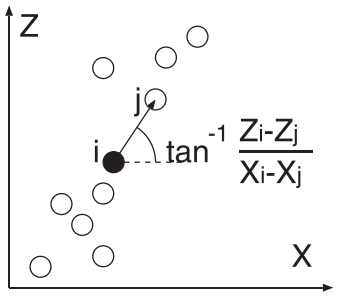

Fig. 2. Schematic of RRPM.

point is calculated by averaging the angle between the i-th and j-th points over all j close to the i-th point. In finding $\hat{\theta}_i$ using (14), we obtain an estimate of the quasi-wavefront orientation. Next, we calculate $Z_X = \tan(\theta_i)$. From this, we can estimate the partial derivative of the i-th range point in terms of X and Y as described in the previous section. Finally, these derivatives are substituted into (3), (4), and (5), to obtain target images.

VI. SHARPNESS METRIC AND SPEED ESTIMATION

In the previous sections, we assumed that the target is stationary during measurement. If the target does not remain still, however, to obtain clear images, the motion of the target must be compensated for. Images obtained with wrongly presumed motion are out of focus and blurred. This feature is used in our proposed method to estimate the motion of a target. The sharpness of an image can be evaluated with the Muller and Buffington (MB) sharpness metric [29, 30].

The fourth-order normalized MB sharpness metric for an image is calculated using

$$h_4 = \frac{\sum_{m=1}^{M} I_m^4}{\left(\sum_{m=1}^{M} I_m^2\right)^2}, \tag{16}$$

where I_m is the m-th pixel of the image, and M is the number of pixels in the image. The following inequality holds for the MB sharpness:

$$\frac{1}{M} \le h_4 \le 1, \tag{17}$$

where the first inequality is a special case of the Cauchy-Schwarz inequality, and the second can easily be proven by expanding the denominator. The first and second terms are equal if and only if all pixels I_m ($m = 1, \ldots, M$) have the same value, whereas the second and third terms are equal if and only if there is a single nonzero pixel, and the remaining pixels are all zeros. If the image is well focused, then the sharpness metric h_4 has a value that is close to 1, which is an important indicator for estimation of the target speed. When we use a three-dimensional image to calculate this metric, the word "pixel" in the above explanation is replaced with the word "voxel."

We assume that the target is moving at a constant velocity, which is a valid assumption within the short measurement time used here. While the limbs of a human target generally move at different speeds from the torso while walking, the head and torso of the target are known to move at an almost constant speed [31]. Because weapons are often hidden on the torso, focusing on the torso alone can be justified. The method that we propose produces multiple images corresponding to various assumed speeds, from which the maximum MB sharpness metric can be used to give an estimate of the actual speed.

In this approach, to evaluate the sharpness of the generated image, the imaging process must be performed repetitively for each assumed speed. Therefore, if the adopted imaging process is slow, this speed estimation method is too time-consuming for practical applications. The use of the proposed fast imaging method, the RRPM, is therefore crucial for application of this speed estimation method in practice.

VII. COMPARISON OF IMAGING METHODS FOR STATIONARY TARGETS

A. Measurement Setup and Imaging Process

We first compare the proposed RRPM with other existing radar imaging methods to evaluate the calculation time and image quality of each method. We selected F-K migration [18] and RPM as the conventional methods for this comparison process.

The parameters we assume in this section are as follows. The distance between the antennas is 5.0 cm in the direction of x, giving $d = 2.5$ cm. The pair of antennas scans from locations ranging from $X_{\min} \le X \le X_{\max}$ and $Y_{\min} \le Y \le Y_{\max}$ at intervals $\Delta_{X,Y}$. The sequence of the antenna scan is as follows:

1) Set x to the initial position $X_{\min}$.
2) Set y to the initial position $Y_{\min}$.
3) Increase y by $\Delta_{X,Y}$.
4) Measure an echo signal at the position.
5) If x reaches the maximum position $X_{\max}$, finish the measurement.
6) If y reaches the maximum position $Y_{\max}$, go to step 2.
7) Otherwise, go to step 3.

Although the choice of scanning sequence does not affect the imaging of a stationary target, the imaging quality of a moving target depends on the choice of sequence. For measurement in this section, $\Delta_{X,Y} = 1$ cm and $X_{\min}$, $X_{\max}$, $Y_{\min}$, and $Y_{\max}$ are -37.0 cm, 37.0 cm, -75.0 cm, and 75.0 cm, respectively. The total number of measuring points is $75 \times 151 = 11325$. The received signals are converted to time-domain data, and background signals are then subtracted. The signals are normalized to the maximum amplitude $\max_{X,Y,Z}|s(X, Y, Z)|$.

For each antenna position, the RPM and RRPM extract 20 peaks ($N = 20$) whose absolute $T_s = 0.05$. We set $\sigma_X = \sigma_Y = 1.0$ cm, $\sigma_Z = 1.0$ cm, and $\sigma_\theta = \pi/100$. The order p of an interference suppressing factor α is set to 4. The i-th target image point (x_i, y_i, z_i) obtained from (3), (4), and (5) is weighted with amplitude $|s_i|$ to generate an image. The

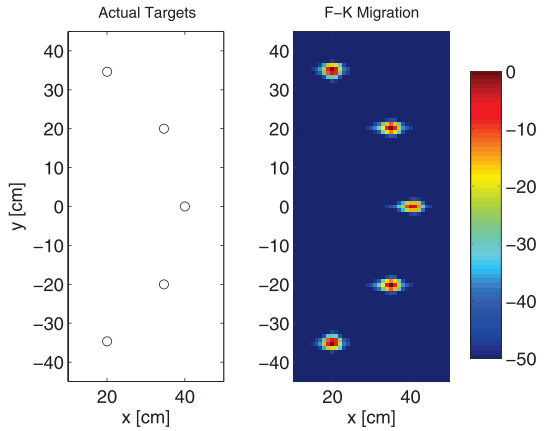

Fig. 3. Actual target positions and image obtained using F-K migration in simulation (in dB).

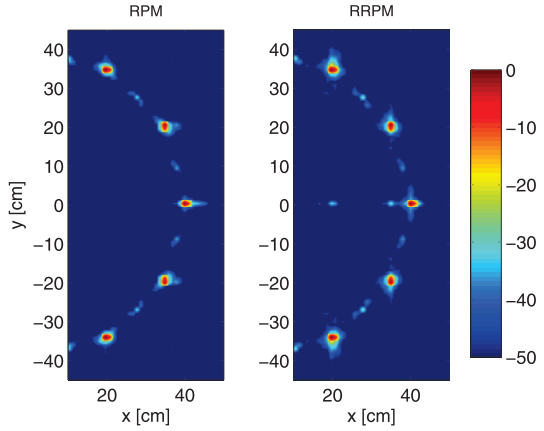

Fig. 4. Images obtained using the RPM and RRPM in simulation (in dB).

generated image is complex valued, and the squared norms of image values constitute the final image in this paper.

B. Imaging Performance Evaluation in Simulations

First, we apply the F-K migration, the RPM, and the proposed RRPM to the simulation data. The simulation data are generated assuming 12 point targets in the plane $z = 50$ cm, equally spaced along a circle with radius of 40.0 cm as shown in the left-hand image of Fig. 3. Here only parts of the targets are shown to illustrate detail. The center frequency is 10.0 GHz and the 3-dB and 10-dB bandwidths are 5.7 GHz and 10.4 GHz.

In this section, the three-dimensional volume image $I_{\mathrm{v}}(x, y, z)$ produced using each imaging method is projected onto the x-y plane as

$$I(x, y) = \int |I_{\mathrm{v}}(x, y, z)| \, \mathrm{d}z \tag{18}$$

to generate a two-dimensional projection image. The two-dimensional projection image obtained using F-K migration is shown in the right-hand image of Fig. 3. The images obtained using the RPM and RRPM are shown on the left- and right-hand sides of Fig. 4. We see that the targets are clearly imaged when using the F-K migration,

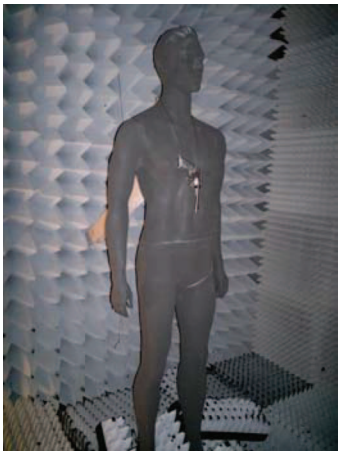

Fig. 5. Experimental setup with mannequin and handgun.

whereas we see cross-terms in the images generated by both the RPM and the RRPM. These cross-terms are generated by interference of the echoes from two adjacent targets, because overlapping waveforms reduce the accuracy in the estimation of $\hat{\theta}$ in (14). In this simulation, the discrete point targets are located in close proximity, which is one of the worst possible scenarios for both RPM and RRPM. In contrast, RRPM generates clear images in measurements for a mannequin and handgun, as shown in later sections. This indicates that the cross-terms do not affect the image quality in practice.

We evaluate the imaging capability using the rms error. As there are 12 point targets, we define the error to be the distance between each image pixel and the closest target. The rms error values for F-K migration, the RPM, and the RRPM are 6.09 cm, 5.25 cm, and 6.98 cm, respectively. The error for the RRPM is larger than that for the RPM because the RRPM is based on an approximation that makes its procedure simpler than that of the RPM. The error for F-K migration is larger than that for the RPM because the artifacts seen in the RPM image are less than –20 dB. Because the difference between the rms errors of the RPM and RRPM is small, RPM is not discussed in later sections of the paper.

C. Imaging Performance Evaluation in Measurements

Next, we apply the methods to experimental data to further verify their performance in realistic scenarios. The data have been acquired in the frequency domain, and Fourier-transformed to obtain time-domain data. We employed an Agilent PNA E8364B sweeping 2001 points at frequencies from 5.0 GHz to 25.0 GHz. The central frequency of the received signals is 13.4 GHz and its 3-dB and 10-dB bandwidths are 2.3 GHz and 14.9 GHz, respectively. The transmitting power is 2.0 dBm. The scan element locations are given in Section VII-A, with the same settings as those used in the simulation (Section VII-B). In our measurements, a mannequin with a conductive surface was placed 50 cm from the antenna scanning plane. Fig. 5 shows our metal-coated mannequin

TABLE I
Measurement Parameters

Lowest frequency	5.0 GHz
Highest frequency	25.0 GHz
Central frequency	13.4 GHz
Transmitting power	2.0 dBm
Antenna gain	10 dBi
Antenna beamwidth	30 deg
Antenna polarization	vertical
xy-positioner resolution	0.01 mm
z-positioner resolution	0.01 mm

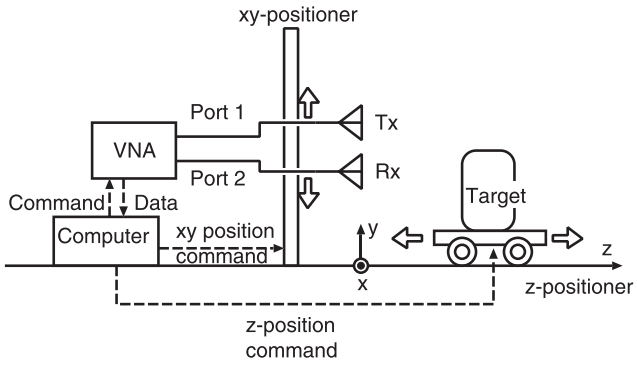

Fig. 6. Diagram showing experimental configuration.

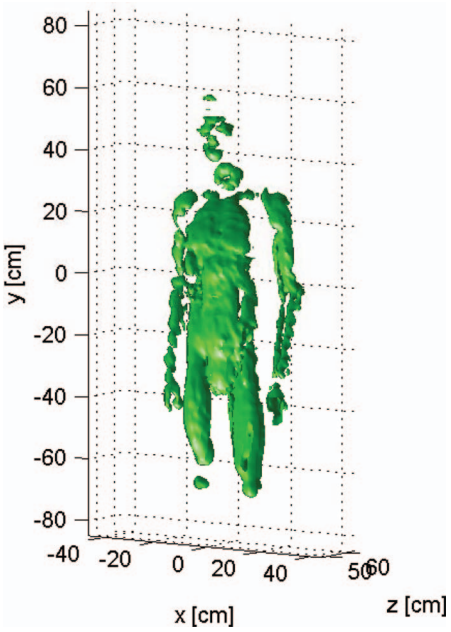

Fig. 7. Three-dimensional surface image generated using F-K migration from measurements taken for mannequin.

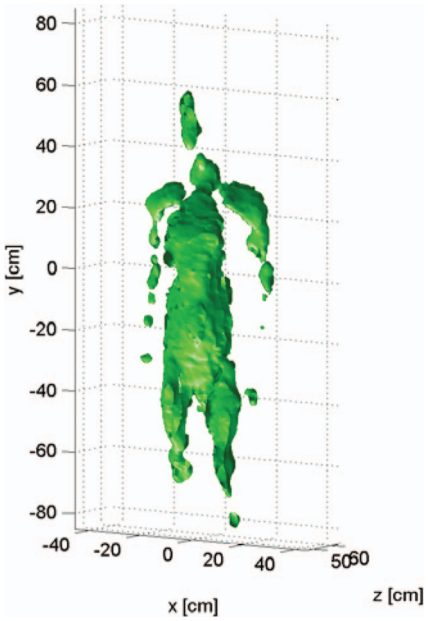

Fig. 8. Three-dimensional surface image generated using proposed RRPM from measurements taken for mannequin.

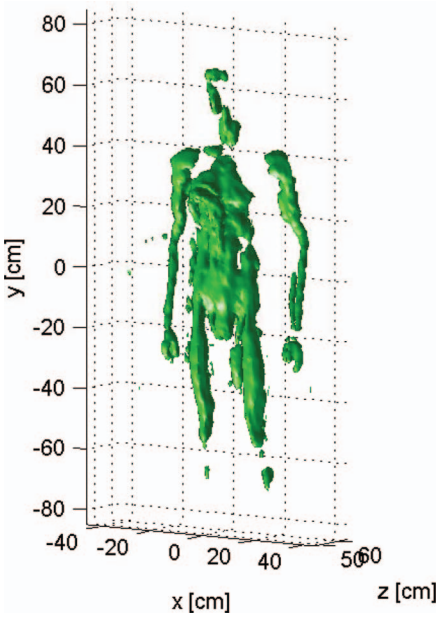

Fig. 9. Image generated using F-K migration from measurement data for mannequin with handgun.

with a handgun used as a target for one of our measurements; the handgun is suspended by a fine thread that does not affect the measurement. We first investigate the imaging performance of the different methods using just the mannequin. Table I shows the parameters used for the experiment. Fig. 6 shows a diagram of the configuration of the experiment.

Figs. 7 and 8 show the images obtained using F-K migration and the RRPM, respectively. Both images successfully depict a human form. We also observe that the image produced using RRPM has part of the arms missing because the weak scattering from the arms are rejected by the thresholding in (1). The image produced using RRPM appears smoother because RRPM exploits the prior information that the target has a clear boundary, whereas F-K migration does not presume any target model.

Next, we applied the methods to the measurement of a mannequin with a handgun. Figs. 9 and 10 show the images obtained with F-K migration and RRPM for a mannequin with a handgun. Although both images reveal a mannequin and handgun, the image produced by RRPM

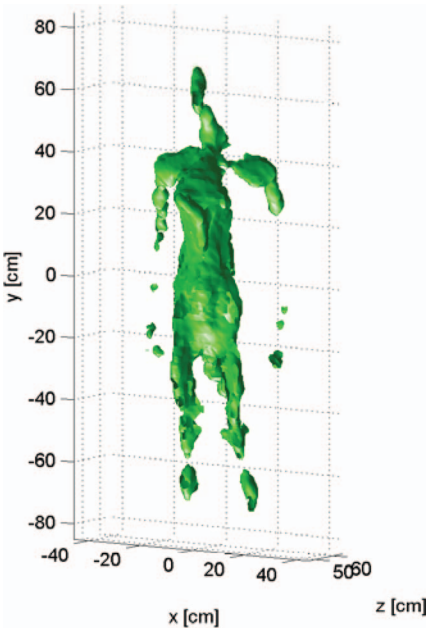

Fig. 10. Image generated using RRPM from measurement data for mannequin with handgun.

TABLE II
Latencies of Instructions

Instruction	Latency	Normalized Latency
FMUL	8	1
FDIV DP	40	5
FSQRT DP	40	5
FSATAN	200-300	25-37.5
FSTAN	240-300	30-37.5

is clearer in terms of identifying the handgun. This result implies that RRPM can be used for weapon detection. However, it should be noted that detection of a weapon in these images might be difficult for a human operator. Therefore, after the radar image is generated, postprocessing will be necessary for automatic weapon detection using a pattern recognition algorithm. However, this postprocessing step is beyond the scope of this paper.

VIII. COMPARISON OF COMPUTATIONAL COMPLEXITY

To compare the speeds of the algorithms, we generally discuss the number of multiplications required in each algorithm. The proposed RRPM algorithm, however, uses division and some elementary functions such as square root, tangent, and arctangent. We therefore estimate the computational complexity of the proposed algorithm based on the processor latency of the x86 architecture [32]. Table II shows the latencies of the instructions used in the proposed RRPM on an Intel processor (ID:0F3H). The table contains floating-point multiplication (FMUL), floating-point division with double precision (FDIV DP), floating-point square root (FSQRT DP), floating-point arctangent (FSATAN), and floating-point tangent

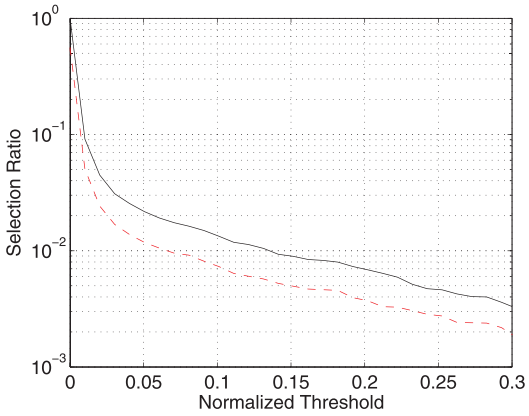

Fig. 11. Selection ratios γ_0 (solid black) and γ (dashed red) calculated from signals received from mannequin with handgun.

(FSTAN). For simplicity, the latencies are normalized relative to that of FMUL, and these values are shown in the right-hand column of the table.

First, let us define N_t as the number of time samples, and N_X and N_Y as the numbers of measurement points in the X and Y directions, respectively. Because the F-K migration requires the FFT to be performed twice, the number of multiplications required is at least $M_{FK} = 2N_X \log_2 N_X N_Y \log_2 N_Y N_t \log_2 N_t$. Specifically, in this experiment, the data have the following sizes: $N_X = 75$, $N_Y = 151$, and $N_t = 5302$. Therefore, the normalized latency of the F-K migration is $M_{\mathrm{FK}} = 6.70 \times 10^{10}$.

In contrast, the RRPM begins with selection of data samples that satisfy (2) and (1) in the time domain. This process reduces the computational load for the RRPM. We define the selection ratios $\gamma_0 = N_{s0}/N_X N_Y N_t$ and $\gamma = N_s/N_X N_Y N_t$ for the number of data samples N_{s0} that satisfy (1), and the number of samples N_s that satisfy both (2) and (1), respectively.

The selection ratio γ_0 can be calculated simply from the statistical properties of the received signal, which can be calculated from the probability density function $p(s)$ of the absolute value of the time-domain data $|s(X, Y, Z)|$ as

$$\gamma_0 = \int_0^{T_s} p(s)\mathrm{d}s. \tag{19}$$

In contrast, to calculate γ, we must also consider the received signal waveforms. As an example, the selection ratios γ_0 and γ are shown in Fig. 11 in black and red, respectively. Both γ_0 and γ were calculated from the data measured for the mannequin with the handgun. In this paper, the threshold T_s has been set at 0.05, which corresponds to values of $\gamma_0 = 0.022$ and $\gamma = 0.012$.

The computational complexity for evaluation of the condition in (2) is $M_0 = 1$, because only one multiplication is needed for each sample that satisfies (1) approximately as

$$\{s(Z) - s(Z - \Delta Z)\}\{s(Z + \Delta Z) - s(Z)\} < 0, \tag{20}$$

where ΔZ is a sampling interval of Z, and the arguments X and Y are omitted for simplicity.

The RRPM method calculates $\hat{\theta}$ using (14) as a summation of the orientations of the neighboring points, where we assume that the number of neighboring points is limited to $N_n \leq 8$ because the weight w decays quickly. We should also note that $w_{i,j}/\sum w_{i,j}$ can be calculated beforehand and stored in a table, because the measurement points and the data samples are discrete. As a result, the calculations required in (14) for each of the neighboring points are four FMULs, two FDIVs, and one FSATAN, which corresponds to $4 + 2 \times 5 + 37.5 = 46$ normalized latencies in the worst case. This calculation is repeated N_n times in the X and Y directions. The total of the normalized latencies for $\hat{\theta}$ is a maximum of $M_1 = 46 \times 8 \times 2 = 736$. Next, FSTAN is performed twice to obtain the derivatives, which adds a maximum of an additional $M_2 = 75$ normalized latencies.

These calculations are followed by application of the bistatic-IBST [(3)–(5)], which is realized using 15 FMULs, two FDIVs, and two FSQRTs by effectively calculating some of the terms that appear multiple times in (3)–(5). The normalized latencies for the bistatic-IBST are represented by $M_3 = 15 + 2 \times 5 + 2 \times 5 = 35$.

In total, the normalized latencies for the RRPM are evaluated to be

$$M_{\mathrm{RRPM}} = N_X N_Y N t \left\{\gamma_0 M_0 + \gamma (M_1 + M_2 + M_3)\right\}. \quad (21)$$

We can therefore calculate the normalized latency of the RRPM $M_{\mathrm{RRPM}} = 6.11 \times 10^8$. In contrast, we can also calculate the normalized latency of the F-K migration to be $M_{\mathrm{FK}} = 6.70 \times 10^{10}$. We therefore concluded that the computational complexity of the RRPM is 110 times smaller than that of the F-K migration. This fast computation property is necessary for estimation of target motion when producing multiple images by assuming various target speeds. When compared with the use of F-K migration in commercial body scanners, the proposed method can produce as many as 110 different images within the same processing time.

All RRPM images shown above were calculated using the same threshold $T_s = 0.05$, which was selected manually. To make the imaging process even faster, we can set a higher threshold T_s. For example, if the threshold is set at $T_s = 0.1$, the selection ratio is then 7.3×10^{-3}, which means that the imaging speed becomes approximately 1.6 times faster than that when $T_s = 0.05$. However, the threshold value also affects the image quality. Fig. 12 shows the image produced using RRPM for the mannequin and the handgun at a higher threshold of $T_s = 0.1$. We see that the shape of the handgun is less clear in the image. Also, the head of the mannequin is missing because the radar cross-section of the head is small, and it is thus rejected by the threshold step from (1).

Therefore, it is important for future studies to develop a method to automatically determine the optimal threshold value by considering the trade-off between computational complexity and image quality. Conventional constant false-alarm rate (CFAR) techniques could be used for this purpose. In most conventional far-field radar detection scenarios, the target type is unknown, the distance to the target varies, and various types of clutter are present. These factors therefore mean that a sophisticated technique is required to determine a threshold. In our application, however, the target is always a human body in free space at a specific distance from the antennas, which dramatically simplifies the process required to set the threshold value.

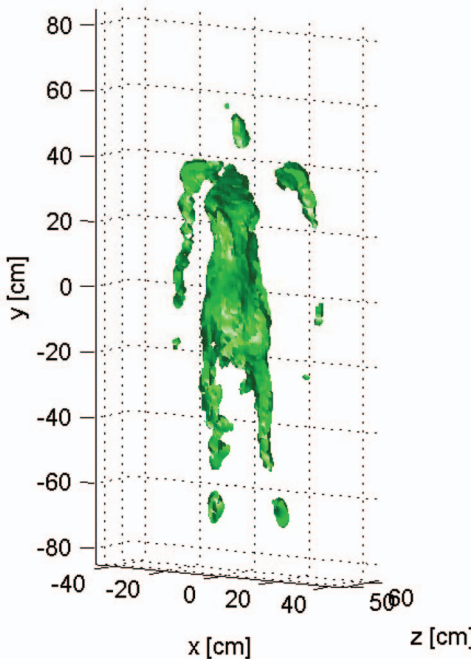

Fig. 12. Image generated using RRPM from measurement data for mannequin with handgun when using higher threshold ($T_s = 0.1$).

IX. PERFORMANCE EVALUATION OF THE TARGET SPEED ESTIMATION METHOD

In this section, we investigate the performance of the proposed method in estimating target speed. We applied the proposed method to measurement data obtained for two types of targets: a dihedral reflector and a handgun. These targets were placed on a horizontal moving platform. We used the same measurement setup as used in the previous section, but with a narrower frequency band from 4.0 GHz to 20.0 GHz with 401 sampling points. The distance between the transmitting and receiving antennas was 5.5 cm, giving d = 2.75 cm. The antennas scanned at intervals of $\Delta_{X,Y} = 1.0$ cm in an area defined by $X_{\min}$, $X_{\max}$, $Y_{\min}$, and $Y_{\max}$ of -25.0 cm, 25.0 cm, -25.0 cm, and 25.0 cm, respectively. The total number of measuring points was thus $51 \times 51 = 2601$. Note that the assumed antenna locations are different to those used for the first experiment in Section VII-C.

The antenna scan sequence was that explained in the previous section while the target moved toward the antenna scanning plane. The target was placed on a moving platform that is controlled electronically. The target scanning length was either 38.0 cm or 19.0 cm,

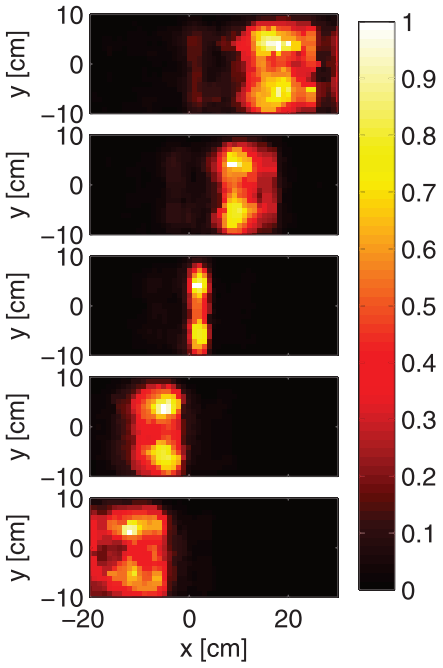

Fig. 13. Images obtained with RRPM for presumed speeds (0.6, 0.8, 1.0, 1.2, and 1.4 m/s from top) for dihedral reflector moving at 1.0 m/s.

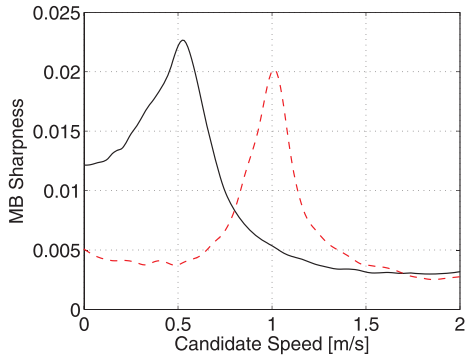

Fig. 14. Sharpness metric for corner reflector moving at two different speeds (actual speeds are 0.5 m/s and 1.0 m/s for black solid and red dashed line).

Fig. 15. Photograph of handgun used in our measurements.

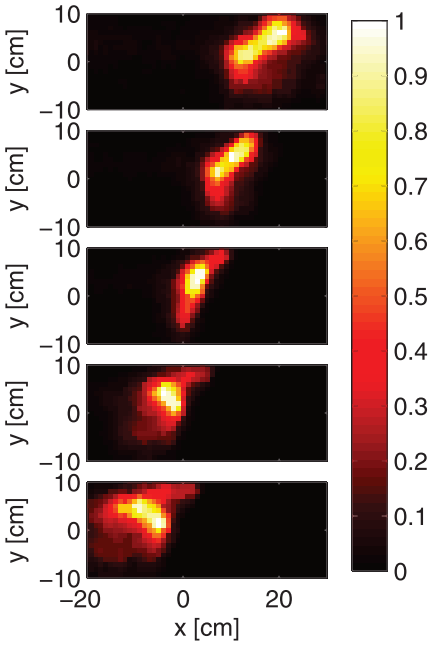

Fig. 16. Images obtained with RRPM for presumed speeds (0.6, 0.8, 1.0, 1.2, and 1.4 m/s from top) for handgun moving at 1.0 m/s.

depending on the assumed target speed. These scenarios corresponded to a target speed of 1.0 m/s and 0.5 m/s, assuming a total measurement time of 0.38 s. In fact, our measurements took longer than the assumed measurement time because we recorded data in the frequency domain.

Fig. 13 shows radar images for the dihedral reflector generated using the RRPM for presuming different speeds; among these, the image corresponding to the actual speed of 1.0 m/s is the sharpest. The target edges are noticeably emphasized in these images, which is because of the characteristics of the IBST, and was discussed by Hantscher et al. in [33]. These characteristics are used to classify targets using their edge locations in [34].

We measured signals from the reflector twice at two different speeds. Fig. 14 shows the MB sharpness metric for various presumed speeds. The position of the peaks clearly shows the correct speeds of the target. The estimated speeds are 0.52 m/s and 1.02 m/s, corresponding to 4% and 2% relative errors. These results indicate that our method can estimate target speeds accurately for simple targets like a reflector.

Next, we applied our method to a handgun. Fig. 15 is a photograph of the handgun used in the measurement. Fig. 16 shows images for the handgun generated using the RRPM for different candidate speeds. Fig. 17 shows the sharpness metric for the handgun moving at 1.0 m/s. The peak of the sharpness metric is seen at 1.03 m/s, giving an accuracy of estimation of 3%. Fig. 18 shows the images generated using the RRPM with true (left) and estimated (right) speeds. Assuming the true speed is known, the first image generated shows a clear image of a handgun; assuming an estimated speed, the second figure also displays a clear three-dimensional outline that is easily recognizable as a handgun. This result indicates that the proposed method can estimate target speeds accurately enough for imaging, and in particular, for applications related to weapon detection.

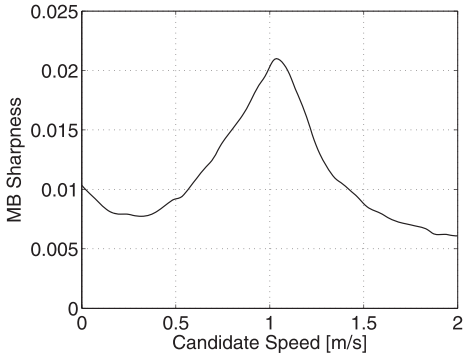

Fig. 17. Sharpness metric for handgun moving at 1.0 m/s (maximum at 1.03 m/s).

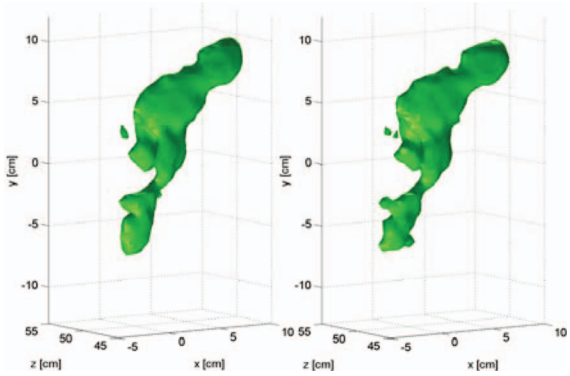

Fig. 18. Estimated target shapes of handgun using actual speed (1.0 m/s, left) and estimated speed (1.03 m/s, right).

X. DISCUSSION

The parameters σ_X and σ_Y are introduced so that we can adjust the local spot size, within which we calculate the orientations of the peak points. If there is only a single target in the far-field, then the orientation of the peak points is independent of the antenna position. In this study, however, there are multiple targets within a near-field, and thus the orientation does depend on the antenna position. For this reason, we calculate the orientations of the points locally by introducing the Gaussian-shaped window that was defined in (6). The values of $\sigma_X = \sigma_Y = 1$ cm used in this study were selected manually.

The parameter σ_θ is introduced to obtain an approximate distribution function for θ by smoothing the discrete orientation values for all combinations of i and j, where the correlation length of the smoothing process is determined by σ_θ. The value of $\sigma_\theta = \pi/100$ was taken from [22].

When the radar measurement aperture size and target distance have been determined roughly, then these parameters can simply be selected and do not need to be updated for each measurement, because the target is always a human body at a certain distance.

In our measurements, we used antennas at 11325 and 2601 positions in Sections VII and IX, respectively. A commercial body scanner, the ProVision (L-3 Communications, NY), performs measurements at more than 128000 positions, as calculated based on the array size (2.0 m), the scanning diameter (1.6 m) and the operating frequency (24.0 GHz). Another body scanner developed by Rohde & Schwartz, Germany, uses 540000 measurements with different combinations of transmitters and receivers at various positions. When compared with these applications, the number of antenna positions used in our study is not particularly large.

XI. CONCLUSION

In this paper, we propose a fast three-dimensional imaging method, the RRPM, for UWB radar systems. The proposed method is a revised version of the conventional bistatic-IBST and the conventional RPM imaging method. The proposed method calculates the relative orientation of the distributed signal peaks employing weighted averaging. We also proposed target speed estimation using the RRPM and MB sharpness metric. We compared the imaging qualities of the proposed RRPM and two conventional methods using simulated and experimental data.

The imaging quality of the proposed RRPM method was shown to be almost the same as that of RPM and F-K migration. The computational complexity of the proposed RRPM method was derived and compared with that of F-K migration, which indicated that the proposed method can produce more than 100 images within the processing time required for F-K migration. This rapid computational capability allows RRPM to be used in the production of an autofocused image of a target in motion, in which the proposed RRPM method is repeatedly applied to produce numerous images while assuming various candidate speeds. We applied the proposed method to the data for a dihedral corner reflector and for a handgun in motion. The target speeds were estimated with errors of 2–4%, which have been shown to be small enough to produce clear images. As a result, we can conclude that the proposed RRPM method will allow us to image a target in unknown motion, and its imaging quality and computational complexity both satisfy the conditions required for security system applications.

ACKNOWLEDGMENT

The authors would like to thank Dr. Timofey Savelyev (Omniradar BV, the Netherlands) for his help and advice with this work.

REFERENCES

[1] Liu, Q., Wang, Y., and Fathy, A. E.
Towards low cost, high speed data sampling module for multifunctional real-time UWB radar.
IEEE Transactions on Aerospace and Electronic Systems, **49**, 2 (2013), 1301–1316.

[2] Colone, F., Falcone, P., Bongioanni, C., and Lombardo, P.
WiFi-based passive bistatic radar: Data processing schemes and experimental results.
IEEE Transactions on Aerospace and Electronic Systems, **48**, 2 (2012), 1061–1079.

[3] Poli, L., Oliveri, G., Rocca, P., and Massa, A.

Bayesian compressive sensing approaches for the reconstruction of two-dimensional sparse scatterers under TE illuminations.
IEEE Transactions on Geoscience and Remote Sensing, **51**, 5 (2013), 2920–2936.

[4] Zhou, H., Sato, M., Takenaka, T., and Li, G.
Reconstruction from antenna-transformed radar data using a time-domain reconstruction method.
IEEE Transactions on Geoscience and Remote Sensing, **45**, 3 (2007), 689–696.

[5] Leigsnering, M., Ahmad, F., Amin, M., and Zoubir, A.
Multipath exploitation in through-the-wall radar imaging using sparse reconstruction.
IEEE Transactions on Aerospace and Electronic Systems, **50**, 2 (2014), 920–939.

[6] Zhang, B., Pi, Y., and Li, J.
Terahertz imaging radar with inverse aperture synthesis techniques: System structure, signal processing, and experiment results.
IEEE Sensors Journal, **15**, 1 (2015), 290–299.

[7] Cooper, K. B., Dengler, R. J., Llombart, N., Thomas, B., Chattopadhyay, G., and Siegel, P. H.
THz imaging radar for standoff personnel screening.
IEEE Transactions on Terahertz Science and Technology, **1**, 1 (2011), 169–182.

[8] Essen, H., Wahlen, A., Sommer, R., Johannes, W., Brauns, R., Schlechtweg, M., and Tessmann, A.
High-wideband 220GHz experimental radar.
Electronics Letters, **43**, 20 (2007).

[9] Keller, P. E., McMakin, D. L., Sheen, D. M., McKinnon, A. D., and Summet, J. W.
Privacy algorithm for cylindrical holographic weapons surveillance system.
IEEE Aerospace and Electronic Systems Maazine, **15**, 2 (2000), 17–24.

[10] Corucci, L., Giusti, E., Martorella, M., and Berizzi, F.
Near field physical optics modelling for concealed weapon detection.
IEEE Transactions on Antennas and Propagation, **60**, 12 (2012), 6052–6057.

[11] Ahmad, F., and Amin, M. G.
Stochastic model based radar waveform design for weapon detection.
IEEE Transactions on Aerospace and Electronic Systems, **48**, 2 (2012), 1815–1826.

[12] Harmer, S. W., Bowring, N., Andrews, D., Rezgui, N. D., Southgate, M., and Smith, S.
A review of nonimaging stand-off concealed threat detection with millimeter-wave radar.
IEEE Microwave Magazine, **13** (2012), 160–167.

[13] Elboushi, A., and Sebak, A.
MMW sensor for hidden targets detection and warning based on reflection/scattering approach.
IEEE Transactions on Antennas and Propagation, **62**, 9 (2014), 4890–4894.

[14] Gumbmann, F., and Schmidt, L.-P.
Millimeter-wave imaging with optimized sparse periodic array for short-range applications.
IEEE Transactions on Geoscience & Remote Sensing, **49**, 10 (2011), 3629–3638.

[15] Hantscher, S., Schlenther, B., Hägelen, M., Lang, S. A., Essen, H., Hülsmann, A., Leuther, A., and Schlechtweg, M.
Security pre-screening of moving persons using a rotating multichannel *W*-band radar.
IEEE Transactions on Microwave Theory and Techniques, **60**, 3 (2012), 870–880.

[16] Wang, G., and Xia, X.-G.
Detection, location, and imaging of fast moving targets using multifrequency antenna array SAR.
IEEE Transactions on Aerospace and Electronic Systems, **40**, 1 (2004).

[17] Martorella, M., Staglianò, D., Salvetti, F., and Battisti, N.
3D interferometric ISAR imaging of noncooperative targets.
IEEE Transactions on Aerospace and Electronic Systems, **50**, 4 (2014), 3102–3114.

[18] Gilmore, C., Jeffrey, I., and LoVetri, J.
Derivation and comparison of SAR and frequency-wavenumber migration within a common inverse scalar wave problem formulation.
IEEE Transactions on Geoscience and Remote Sensing, **44**, 6 (2006).

[19] Winters, D. W., Shea, J. D., Madsen, E. L., Frank, G. R., Van Veen, B. D., and Hagness, C.
Estimating the breast surface using UWB microwave monostatic backscatter measurements.
IEEE Transactions on Biomedical Engineering, **55**, 1 (Jan. 2008), 247–256.

[20] Salman, R., and Willms, I.
In-wall object recognition based on SAR-like imaging by UWB-radar.
In *Proceedings of 8th European Conference on Synthetic Aperture Radar (EUSAR)*, June 2010.

[21] Kidera, S., Kani, Y., Sakamoto, T., and Sato, T.
A fast and high-resolution 3-D imaging algorithm with linear array antennas for UWB pulse radars.
IEICE Transactions on Communications, **E91-B**, 8 (Aug. 2008), 2683–2691.

[22] Kidera, S., Sakamoto, T., and Sato, T.
Accurate UWB radar 3-D imaging algorithm for complex boundary without range points connections.
IEEE Transactions on Geoscience and Remote Sensing, **48**, 4 (Apr. 2010), 1993–2004.

[23] Sakamoto, T., Savelyev, T. G., Aubry, P. J., and Yarovoy, A. G.
Revised range point migration method for rapid 3-D imaging with UWB radar.
In *Proceedings of 2012 IEEE International Symposium on Antennas and Propagation and USNC-URSI National Radio Science Meeting*, July 2012.

[24] Sakamoto, T., Savelyev, T. G., Aubry, P. J., and Yarovoy, A. G.
Fast range point migration method for weapon detection using ultra-wideband radar.
In *Proceedings of European Radar Conference*, Nov. 2012.

[25] Sakamoto, T., Savelyev, T. G., Aubry, P. J., and Yarovoy, A. G.
High-resolution weighted range point migration method for fast 3-dimensional imaging with ultra wideband radar.
In *Proceedings of IEEE Radar Conference 2013*, May 2013.

[26] Salman, R., Willms, I., Sakamoto, T., Sato, T., and Yarovoy, A. G.
Environmental imaging with a mobile UWB security robot for indoor localisation and positioning applications.
In *Proceedings of IEEE Radar Conference 2013*, May 2013.

[27] Sakamoto, T., Sato, T., Aubry, P., and Yarovoy, A.
Target speed estimation using revised range point migration for ultra wideband radar imaging.
In *Proceedings of European Conference on Antennas and Propagation (EuCAP) 2013*, 2013.

[28] Salman, R., and Willms, I.
3D UWB radar super-resolution imaging for complex objects with discontinuous wavefronts.
In *Proceedings of 2011 IEEE International Conference on Ultra-Wideband*, Sept. 2011, 346–350.

[29] Muller, R. A., and Buffington, A.
Real-time correction of atmospherically degraded telescope images through image sharpening.
Journal of the Optical Society of America, **64**, 9 (Sept. 1974), 1200–1210.

[30] Fienup, J. R., and Miller, J. J.
Aberration correction by maximizing generalized sharpness metrics.

Journal of the Optical Society of America, **20**, 4 (Apr.. 2003), 609–620.

[31] van Dorp, P., and Groen, F. C. A.
Human walking estimation with radar.
IEE Proceedings - Radar, Sonar and Navigation, **150**, 5 (2003).

[32] *Intel 64 and IA-32 Architectures Optimization Reference Manual*.
Intel Corporation, CA, 2014.

[33] Hantscher, S., Praher, B., Reisenzahn, A., and Diskus, C. G.
Comparison of UWB target identification algorithms for through-wall imaging applications.
In *Proceedings of 3rd European Radar Conference*, 2006, 104–107.

[34] Damyanov, D., Schultze, T., Willms, I., and Salman, R.
Super-resolution feature extraction imaging algorithm for complex objects.
In *Proceedings of IEEE International Conference on Ultra-WideBand*, 2014, 207–210.

Takuya Sakamoto (M'04) received the B.E. degree in electrical and electronic engineering from Kyoto University, Kyoto, Japan, in 2000 and the M.E. and Ph.D. degrees in communications and computer engineering from the Graduate School of Informatics, Kyoto University, in 2002 and 2005, respectively.

Since 2015, he has been an Associate Professor at the Graduate School of Engineering, University of Hyogo, Himeji, Japan. He is also a Researcher at the Graduate School of Informatics, Kyoto University, Kyoto, Japan. From 2006 through 2015, he was an Assistant Professor at the Graduate School of Informatics, Kyoto University. From 2011 through 2013, he was also a Visiting Researcher at Delft University of Technology, Delft, The Netherlands. His current research interests lie in ultra-wideband radar, radar imaging, and radar signal processing.

Dr. Sakamoto is a member of the Institute of Electronics, Information and Communication Engineers of Japan (IEICE), the Institute of Electrical Engineers of Japan (IEEJ), and the Japan Society of Ultrasonics in Medicine. He has been serving as a Treasurer of IEEE AP-S Kansai Chapter since 2015.

Toru Sato (M'92) received the B.E., M.E., and Ph.D. degrees in electrical engineering from Kyoto University, Kyoto, Japan, in 1976, 1978, and 1982, respectively.

He has been with Kyoto University since 1983 and is currently a Professor in the Department of Communications and Computer Engineering in the Graduate School of Informatics. His major research interests have included system design and signal processing aspects of atmospheric radar, radar remote sensing of the atmosphere, observations of precipitation using radar and satellite signals, radar observation of space debris, and signal processing for subsurface radar signals.

Prof. Sato is a member of the Institute of Electronics, Information, and Communication Engineers of Japan, the Society of Geomagnetism and Earth, Planetary and Space Sciences, the Japan Society for Aeronautical and Space Sciences, and the American Meteorological Society. He was awarded the Tanakadate Prize in 1986.

Pascal J. Aubry received the D.E.S.S. degree in electronics and automatics from the Université Pierre et Marie Curie (Paris 6), Paris, France, in 1993.

He was a Young Graduate Trainee with the European Space Research and Technology Centre (ESTEC) in 1996, where he was involved in antenna measurements. Since 1997, he has been with the International Research Centre for Telecommunications and Radar, Delft University of Technology (TUD), Delft, The Netherlands. His research interests include antenna measurement techniques, radar system testing, and signal processing and analysis.

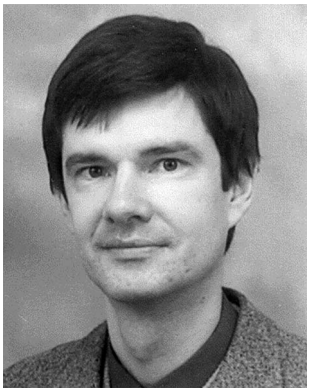

Alexander G. Yarovoy (M'96–SM'04–F'15) received the Diploma (with honor) in radiophysics and electronics from the Kharkov State University, Kharkov, Ukraine, in 1984. He received the Candidate Phys. & Math. Sci. and Doctor Phys. & Math. Sci. degrees in radiophysics from the Kharkov State University, Kharkov, Ukraine in 1987 and 1994, respectively.

In 1987, he joined the Department of Radiophysics at the Kharkov State University as a Researcher and became a Professor there in 1997. From September 1994 through 1996, he was with the Technical University of Ilmenau, Ilmenau, Germany, as a Visiting Researcher. Since 1999, he has been with the Delft University of Technology, Delft, The Netherlands. Since 2009, he has been the Chair of Microwave Sensing, Systems and Signals. His main research interests are in ultrawideband (UWB) microwave technology and its applications (particularly radar) and applied electromagnetics (particularly UWB antennas).

Dr. Yarovoy has authored and coauthored more than 250 scientific or technical papers, four patents, and 14 book chapters. He served as a Guest Editor for five special issues of IEEE Transactions and other journals. Since 2011, he has been an Associated Editor of the *International Journal of Microwave and Wireless Technologies*. He was the recipient of the European Microwave Week Radar Award for the paper that best advances the state-of-the-art in radar technology in 2001 (together with L. P. Ligthart and P. van Genderen) and again in 2012 (together with T. Savelyev). In 2010, together with D. Caratelli, he received the Best Paper Award from the Applied Computational Electromagnetic Society. He served as the Chair and Technical Program Committee Chair of the 5th European Radar Conference (EuRAD'08), Amsterdam, The Netherlands, as well as the Secretary of the 1st European Radar Conference (EuRAD'04), Amsterdam. He served also as the Cochair and TPC Chair of the 10th International Conference on GPR (GPR2004) in Delft. Since 2008, he has served as the Director of the European Microwave Association.